

Accepted manuscript

© <2017>. This manuscript version is made available under the CC-BY-NC-ND 4.0 license

<http://creativecommons.org/licenses/by-nc-nd/4.0/>

The full article can be accessed through: <https://doi.org/10.1016/j.matdes.2016.10.035>

Accepted manuscript

**Influence of testing orientation on mechanical properties of Ti45Nb deformed
by high pressure torsion**

B. Völker^{1)*}, N. Jäger¹⁾, M. Calin²⁾, M. Zehetbauer³⁾, J. Eckert^{1),4)} and A. Hohenwarter¹⁾

¹⁾ Department of Materials Physics, Montanuniversität Leoben, 8700 Leoben, Austria

²⁾ Institute for Complex Materials, IFW Dresden, P.O. Box 270116, D-01171 Dresden,
Germany

³⁾ Physics of Nanostructured Materials, Faculty of Physics, University of Vienna, A-1090
Vienna, Austria

⁴⁾ Erich Schmid Institute of Materials Science, Austrian Academy of Sciences, 8700
Leoben, Austria

* Corresponding Author: bernhard.voelker@unileoben.ac.at

Abstract

Ti45Nb is a promising choice as an implant material due to its low Young's modulus and its good biocompatibility, however the material's strength is relatively low in the conventionally coarse-grained state. Recently, severe plastic deformation was suggested to improve the mechanical properties of such materials. In this study the influence of the testing direction on the mechanical properties including strength, ductility and fracture toughness is investigated using relatively large HPT samples with a diameter of ~30 mm and a thickness of ~7 mm. It is shown that especially the strength and fracture toughness develop a pronounced orientation dependence. With respect to the testing direction, the strength increased from ~400 MPa in the coarse-grained state to around 950 to 1050 MPa after deformation and the fracture toughness remains quite high with values between 75 and 110 MPam^{1/2}. Hence, the deformed Ti45Nb alloy represents an alternative to other Ti-alloys recently used as implant materials with the major advantage of having a low Young's modulus combined with high strength and fracture toughness.

Keywords: High pressure torsion; severe plastic deformation; beta-titanium alloys; fracture toughness; Young's modulus; implants

Introduction

Ti and its alloys have been used as implant materials for many years because of certain aspects which make Ti-based materials advantageous for this application, such as high corrosion resistance and excellent biocompatibility [1-4]. Furthermore, various Ti-alloys possess beneficial mechanical behavior, which makes them a good choice for load bearing implants. Even though the Young's modulus of conventional Ti-alloys is still more than 3 times higher than that of bone with 10-30 GPa [1-4] it is significantly lower than the one of other materials considered for implants, such as stainless steels or CoCr alloys [1,4]. The difference in the modulus results in a significant stress shielding effect [5-7] between implant and bone. The stress shielding leads to bone resorption and thus, a reduction in the load bearing capability strength of the bone, which can lead to a loosening of the implant in the bone [8,9]. Another class of Ti-alloys is recently gaining more interest in this context, namely β -Ti alloys which have a considerably lower Young's modulus than α - and $\alpha+\beta$ -Ti alloys. A prominent representative of β -Ti alloys is Ti45Nb, because it is one of two alloy compositions in the Ti-Nb system with a significantly lower Young's modulus compared to conventional Ti-alloys [10-13]. The drawback of β -Ti alloys is their low strength compared to other implant alloys [4,14,15] making them unsuitable for load bearing applications. Recently, it has been tried to increase the strength of β -Ti alloys using intense work hardening [3,15] and especially severe plastic deformation (SPD) techniques [16-19] showed promising results for Ti based materials [3,20-25]. When SPD techniques are used, it has to be taken caution that no additional phases form during deformation, like in the case of pure α -Ti, which forms ω -Ti under high hydrostatic pressures having a higher Young's modulus than α -Ti [3,26,27]. Despite this, the presence of high hydrostatic pressures during SPD is often desired as it enables large deformation strains by suppressing crack formation and this is best fulfilled by the high pressure torsion (HPT) process [12,13]. In the case of Ti45Nb it could already been shown that by using HPT the strength can be significantly increased and that the high compressive stress during HPT has no influence on the Young's modulus [28].

So far the studies on HPT-processed Ti45Nb have been restricted to fairly small samples with diameters of 8 mm and thicknesses less than 1 mm. For future applications of HPT-processed materials, for example dental implants, larger material dimensions will be required. Moreover, in previous studies on SPD-processed metals it has been shown that especially the fracture toughness, which can be used to characterize the damage tolerance of

an implant and thus the resistance against crack growth, may exhibit a pronounced orientation dependence [29,30]. Therefore, the present work focuses on the technical feasibility of processing larger HPT-disks of Ti45Nb and to investigate the influence of the testing orientation on the mechanical properties of Ti45Nb deformed by HPT [31–34].

Materials and Methods

The as-received material of Ti45Nb was in a hot-extruded state. The chemical composition in weight% was as follows: Nb: 44.94, Fe: <0.03, Cr:<0.01, Mn:<0.01, Mg<0.01, Si: <0.1, K<0.01, Na<0.01, O<0.095, N<0.007. To determine the initial microstructure of the as-received material electron backscatter diffraction (EBSD) images with a Zeiss Leo 1525 scanning electron microscope (SEM) were recorded. From the as-received material disks with 30 mm diameter and a thickness of 11 mm were prepared. These disks were pre-loaded under a pressure of 5 GPa. Afterwards the pre-loaded disks were sandblasted, followed by HPT deformation. The experiments were performed with a pressure of 5.7 GPa, 15 revolutions were applied and the time for one revolution was 15 minutes in order to avoid a significant increase of temperature. To investigate the homogeneity of the HPT-disks in terms of hardness Vickers hardness measurements along the radius and across the thickness of the HPT disks were performed on a Buehler MicroMet 5104, with a load of 500 gf. All mechanical samples were prepared using material only from disk areas where the hardness saturated during deformation and was constant along the radius in the middle plane of the disks, as also discussed in more detail later in Fig. 3. From these areas compact tension C(T) specimens and tensile samples were prepared. The C(T) samples have different orientations and are named after the designated crack propagation direction including a shear, axial and radial specimen orientation, see Fig. 1a.

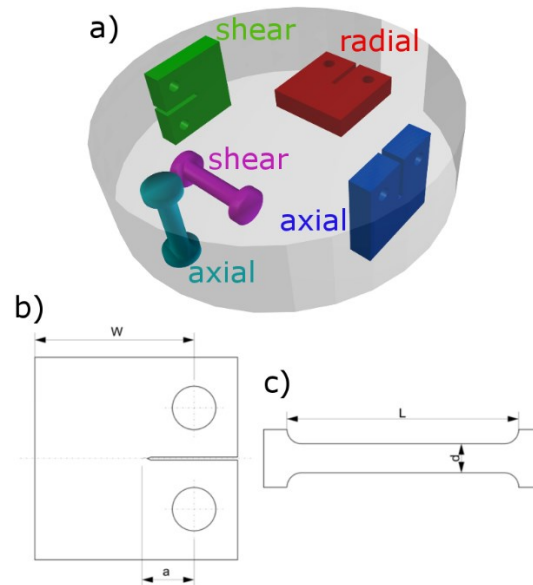


Figure 1 a) Orientation of the different compact tension (CT) and tensile samples extracted from the HPT disk. b) Geometry of the C(T) samples. c) Geometry of the tensile samples having a diameter d of about 500 μm and a gauge length of about 3 mm.

The geometry was machined in accordance to ASTM E399 [35]. The C(T) specimens had a width, W , of ~ 5.2 mm, a crack length, a , of ~ 2.6 mm and a thickness, B , of approximately 2.6 mm (see also Fig. 1b). The samples were notched using a diamond wire saw and a razorblade with a 6 μm diamond paste. The initial fatigue pre-crack was introduced by cyclic compression-compression loading. Testing of the CT-samples was carried out on a Kammrath & Weiss tensile module with a loading rate of 2.5 $\mu\text{m/s}$. The measuring procedure and data evaluation was performed with reference to the same ASTM E399 standard. Tensile samples were prepared from the saturation region of the HPT disk as well. Two orientations were tested, the shear- and axial-direction (see Fig. 1) with 3 specimens respectively. To produce these samples a grinding method introduced by Rathmayr et al. [36] was utilized. The round samples had a testing length of 3 mm and a diameter of 0.5 mm. The testing of the tensile samples was performed on a Kammrath & Weiss tensile module with a testing speed of 2.5 $\mu\text{m/s}$. Displacement measurement was done by an optical image correlation method developed by Rathmayr et al. [36].

The crack tip opening displacement for crack initiation (CTOD_i) was determined as another measure for fracture toughness and was recorded at the transition from the fatigue pre-crack to the final fracture surface. For that purpose, 3D-reconstruction of the fracture surfaces were performed and then line-profiles were extracted to re-construct the fracture

process and to measure in this way CTOD_i. Details to this technique can be found elsewhere [37,38]. From the measured CTOD a critical stress intensity can be derived with following relation [39]:

$$K_{IC} = \sqrt{\frac{mCTOD_i \sigma_y E}{(1 - \nu^2)}} \quad (1)$$

Here σ_y represents the measured yield stress, E the Young's Modulus of about 64 GPa [11–13], m a dimensionless constant with 2 and ν is the Poisson's ratio which is estimated with 0.3.

TEM samples of the saturation regime were prepared in the conventional way by grinding, dimpling and final Ar-ion thinning to electron transparency. The diffraction pattern was recorded on a Phillips CM12 transmission electron microscope (TEM) with 120 kV acceleration voltage. The scanning TEM (STEM) images were taken on a JEOL 2100F image-side C_s-corrected microscope.

Experimental results and discussion

The as-received material is presented in Fig. 2 showing an equiaxed microstructure, which was revealed by EBSD-measurements in the SEM, with a mean grain size of 40 μm . The measurements clearly prove the single-phase character of Ti45Nb consisting exclusively of the bcc β -Ti phase. In addition, a pronounced texture of the recrystallized material can be recognized.

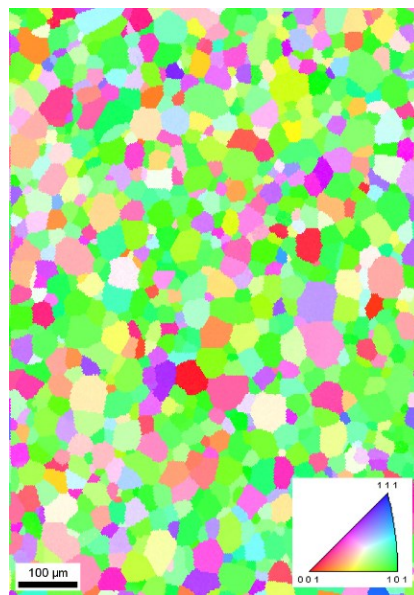


Figure 2 Inverse pole figure map of the as-received material.

Vickers hardness measurements on a cross-section of the deformed HPT disk were utilized to probe the variation in hardness along the radius and across the thickness. In Fig. 3 the hardness within the disk along the radius for different planes across the thickness of the disk is summarized.

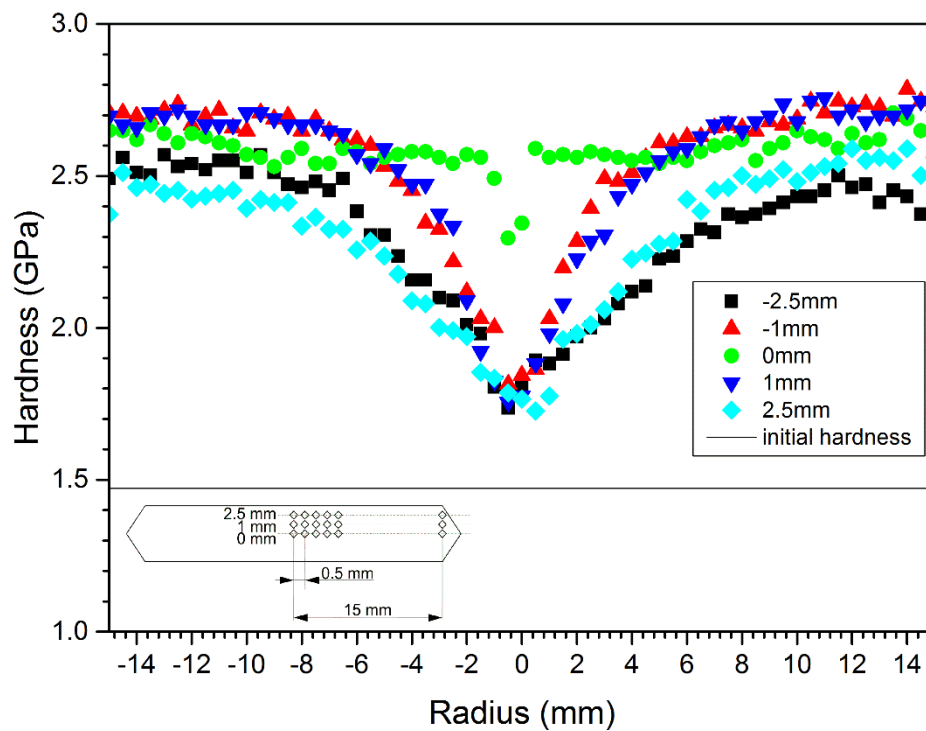


Figure 3 Hardness measurements performed on the deformed HPT disk. Hardness measurements were performed along the radius from the center to the edge and across the thickness of the disk. The inset image represents the cross-section of the disk showing the planes and their distance from the middle plane along which the hardness was tested. The saturation regime with about 2.6 GPa for the middle plane of the disk is reached in about 1 mm radial distance from the center.

Focusing at first onto the middle plane (0 mm) it can be seen that the hardness is very uniform with a hardness of approximately 2.6 GPa except for the very center for radii smaller than 1 mm. For comparison the hardness of the undeformed material is about 1.5 ± 0.02 GPa. A distinctive variation of the hardness distribution in the axial direction of the HPT-disk can be observed as well. For the ± 1 mm planes the saturation regime is reached at larger radii at about ± 5 mm and for the ± 2.5 mm planes the maximum hardness saturates at radii of about ± 7 mm. These results show that with increasing distance from the middle plane the onset of the saturation is reached at a larger radius and the saturation hardness decreases slightly. Similar hardness values and consequently microstructural variations have been observed

before [40,41]. It was found that the ratio of thickness to diameter, t/d , of the HPT-disks controls the axial homogeneity and should not exceed a certain limit which is about 1/13 or smaller, whereas in the present case t/d is about 1/5. Even though the disk is not fully uniform in the axial direction the variation is small with about 0.2 GPa between the middle plane and the edges of the sample and the increase in hardness compared to the undeformed material is large. The radial homogeneity could possibly be improved by increasing the number of rotations. The axial homogeneity could be improved by changing the t/d ratio. Nevertheless, with the knowledge of the hardness distribution of the present HPT-disk geometry implants can be extracted from mechanically adequate areas of the disks or can even possess an intentionally adjusted microstructural gradient.

STEM images of the HPT disk after deformation, from the saturation regime, are depicted in Fig. 4, looking into the radial direction. Elongated grains are visible with a thickness of about 50 nm. In contrast to the thickness, it is difficult to measure the length of the grains quantitatively, see Fig. 4.

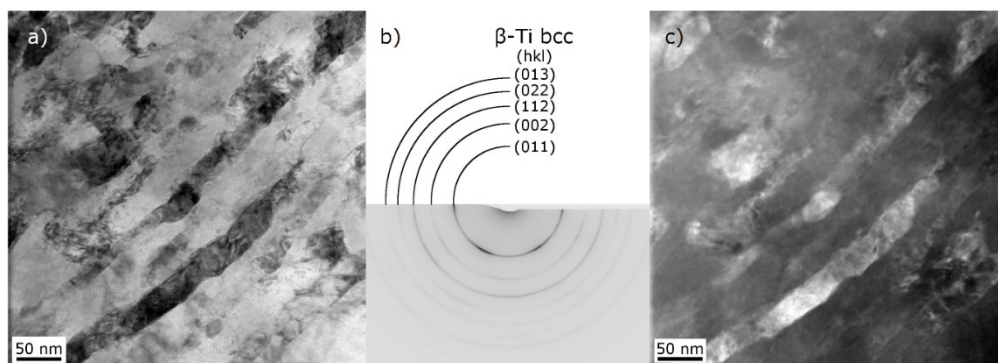


Figure 4 In a) a bright-field STEM image and in c) a HAADF STEM image of the saturation region are depicted. Both images show the as-deformed state after the HPT deformation with elongated grains which have a thickness of about 50 nm. In b) the diffraction pattern of the as-deformed state is depicted, which shows a single phased β -Ti bcc structure.

Additional orientation measurements with TEM were used to estimate their length yielding a value between 200 and 300 nm. The electron diffraction image after the HPT deformation (Fig. 4b) shows rings, which prove the polycrystalline single-phase nature of the microstructure. All rings in the diffraction pattern correspond to a bcc crystal structure with a lattice constant of about 0.329 nm. This is in good accordance to literature values (0.3282 nm [42]). Since all Debye-Scherrer rings belong to a bcc-sequence it is proven that the material remains single phased after HPT deformation.

The presented microstructure is typical of HPT-processing when specimens are inspected into the radial direction. It was found that the grain length parallel to the shear direction is strongly dependent on the deformation temperature yielding larger aspect-ratios for lower deformation temperatures [43]. Since Ti-alloys have in general high melting points, room-temperature deformation represents a low homologous deformation temperature leading to this high aspect-ratio of the grains, which is strongest pronounced in this viewing direction. The majority of HPT-studies are normally based on very thin disks making it technically easier to investigate the microstructure parallel to the rotation axis. However, in this direction the grain elongation is less pronounced on account of the typical pan-cake structure of SPD-deformed grains.

Tensile tests were conducted to compare the strength of the as-received material with the strength of the HPT deformed material. The results of the experiments are listed in *Table 1* and representative examples of tensile tests are shown in Fig. 5.

Table 1 Summary of the results of the tensile test. $R_{p0.2}$ represents the yield strength, R_m the ultimate tensile strength, A_m the uniform elongation and A_f the elongation to fracture. The values represent average numbers of 3 measurements and as an error the standard deviation is given.

Orientation	as-received	axial	shear
$R_{p0.2}$ (MPa)	354±38	800±25	896±52
R_m (MPa)	418±41	948±28	1046±26
A_m (%)	6.8±0.2	1.3±0.3	1.4±0.1
A_f (%)	13.8±0.2	7.1±1.0	7.6±1.1

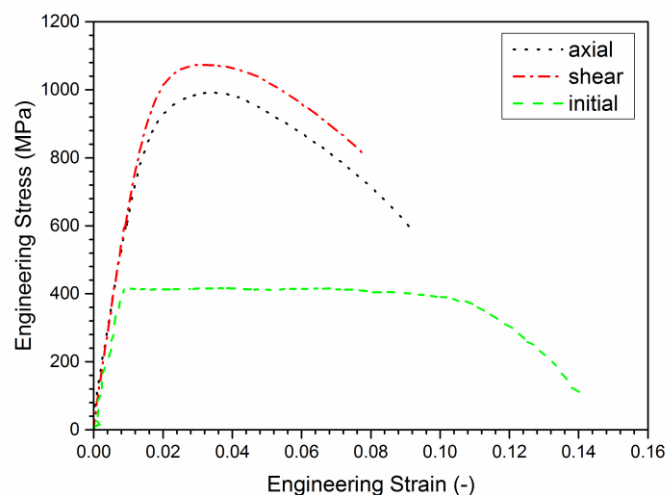


Figure 5 Stress-strain curves for the as-received state and the HPT-deformed state in two directions (axial and shear). A significant increase in strength is seen for the as-deformed samples compared to the initial state.

The as-received material showed a strength of about 420 MPa and a maximum elongation of 14%. After HPT-processing the strength in terms of flow stress and ultimate strength shows an exceptional rise combined with a distinctive influence of the testing direction. The measurements reveal in the axial direction an ultimate tensile strength of approximately 950 MPa and in shear direction about 1050 MPa. The significant increase in strength is accompanied with a decrease in ductility, which is also observed for other materials [20,31,44–46]. In another investigation similar strength levels for the investigated Ti45Nb were revealed after HPT deformation [10,28]. The orientation influence of the strength may be a consequence of the texture induced by the HPT process, which was found to be only weakly pronounced in preceding studies [28]. The tensile tests also reveal a loss of ductility in the HPT deformed samples, however with no significantly measurable orientation dependence, see Tab.1. The decrease in ductility seems to be an acceptable trade-off in comparison with the exceptional gain in strength. Interesting to note is that a significant amount of hardening occurs in the SPD-deformed state quite in contrast to the coarse-grained as-received material. The almost ideal plastic behavior, of the coarse-grained state is similar to that observed in Gum Metal [47].

Finally, the orientation dependence of the fracture toughness of the HPT deformed material was investigated. The fracture toughness was calculated according to the recommendations of the ASTM E399-90 and important measures are presented in Tab. 2.

Table 2 Overview of the fracture toughness results for different testing orientations: Calculated fracture toughness value K_Q according to ASTM E399-90, the maximum fracture toughness, K_{max} , derived from the maximum load, the force-ratio, P_{max}/P_Q , of maximum force and the force used for K_Q -calculation, the crack tip opening displacement for crack initiation ($CTOD_i$) and fracture toughness, K_{IC} , calculated from $CTOD_i$.

Orientation	axial	radial	shear
K_Q (MPa \sqrt{m})	21	25	42
K_{max} (MPa \sqrt{m})	61	58	64
P_{max}/P_Q (-)	2.9	2.3	1.5
$CTOD_i$ (μm)	40	106	49
K_{IC} (from $CTOD$) (MPa \sqrt{m})	74	109	78

Using the approach described in the standard, the axial and radial directions have a similar provisional fracture toughness, K_Q , with values of 21 MPam^{1/2} and 25 MPam^{1/2}, respectively. These two directions showed, in comparison to the shear direction, with 42

MPam^{1/2}, almost a factor of 2 lower value. However, none of the three orientations fulfill the requirements for linear elastic fracture mechanics as the ratio of the maximum load, P_{max} , and the load used for the fracture toughness calculation, P_Q , is larger than 1.1, see Tab.2. This indicates excessive plastification of the specimen and the loss of small scale yielding conditions.

As a result, CTOD_i-measurements were performed and examples of the measurements for all three orientations are shown in Fig. 6.

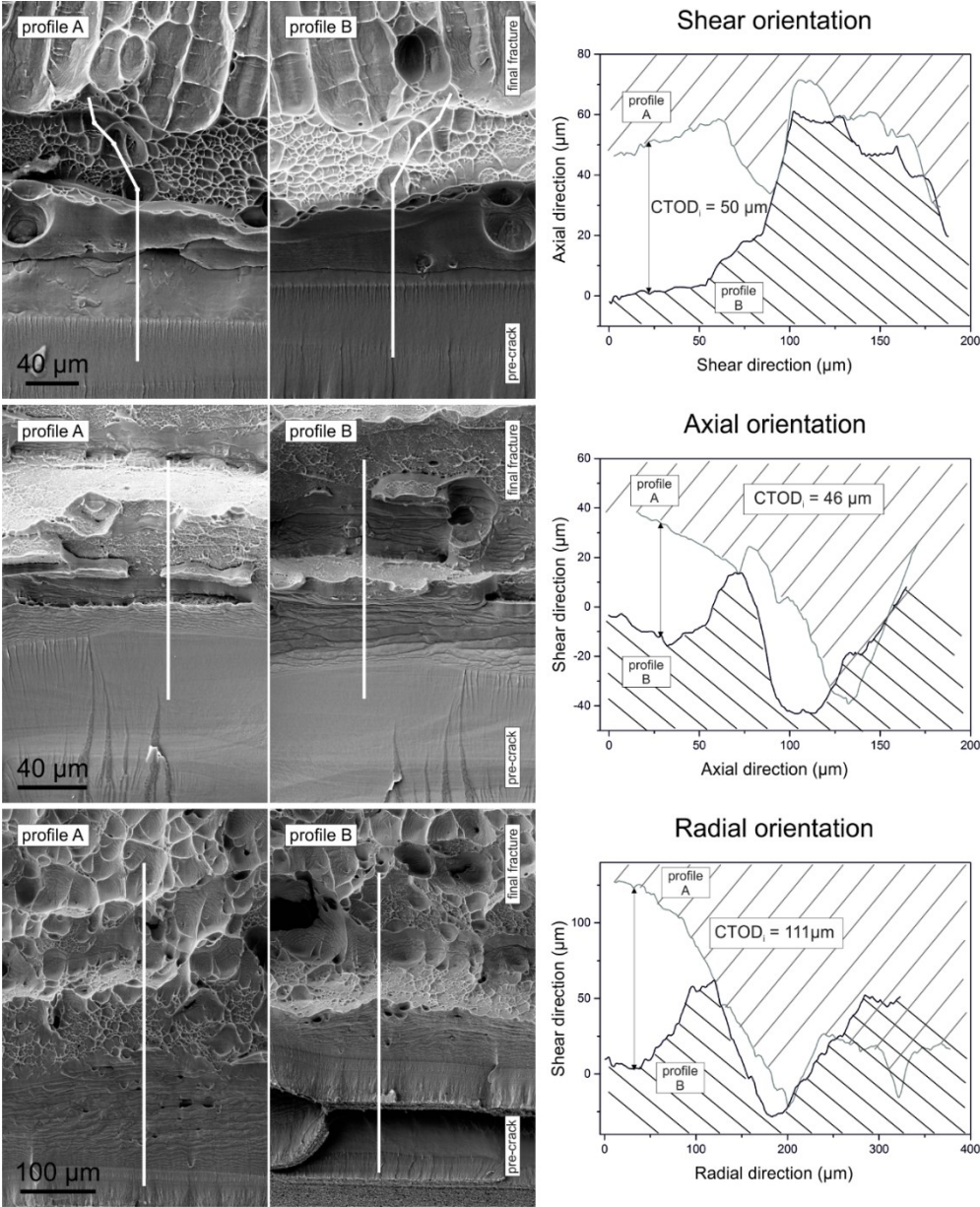


Figure 6 Examples of CTOD_i measurement for all three testing orientations taken at the crack initiation site. Comparison of fractographs taken from the two halves of the broken specimen at the same position with indicated identical crack paths along which the CTOD_i was measured (left sides). Arrangement of the crack profiles at the point prior to coalescence of first void defining CTOD_i.

For all three orientations the corresponding K_{IC} were then evaluated with *Eq. 1*. The average CTOD_i-values of at least three measurements and the resulting K_{IC} for the different orientations are listed in Tab.2. The CTOD-measurements deliver much higher fracture toughness values and reveal a different orientation dependence of the fracture toughness than the invalid ASTM-evaluation.

Nevertheless, the stress-based *K*-analysis according to the standard was incorporated in this paper in order to exemplify that when small scale yielding conditions are lost only lower bound values for the fracture toughness would be measured. This is a frequent problem when it is attempted to measure fracture toughness on ductile materials with too small specimen dimensions. Since the use of the standard on such small samples underestimates the fracture toughness of the material drastically, only the fractography-based CTOD_i-measurements represent an useful fracture toughness evaluation, which is not geometry dependent and a real material parameter.

The fracture toughness depends on the orientation of the sample in the HPT disk, with 74 MPam^{1/2} in axial, 78 MPam^{1/2} in shear and 109 MPam^{1/2} in the radial orientation. The evaluated fracture toughness values are, in comparison to other Ti based materials after similar deformation processes [48,49], significantly higher. The undeformed Ti45Nb-alloy has a higher fracture toughness of about 150 MPam^{1/2} [50], however at the expense of a much lower strength. Unexpectedly shear and axial orientation have more or less the same fracture toughness, which is surprising as the strong grain alignment as presented in Fig. 4, could suggest a distinctive anisotropy. Strong anisotropies were found before in bcc-metals subjected to HPT, for example for iron [29]. In iron intergranular fracture along the elongated grain structure prevailed and lead to a pronounced anisotropy in the fracture behavior between the shear and axial orientation. In axial orientation the fracture resistance was found to be much higher and therefore the crack deflected and propagated again along the elongated grain boundary structure exhibiting the lower fracture resistance. In the present case ductile failure prevails in the shear and axial orientation as shown in Fig. 6, which seems to be the origin for a similar fracture resistance in both orientations. This is also reflected by the fact that the crack for the axial orientation does not show a strong crack deflection commencing from the pre-crack as found for example in iron. In general, the dimple size found in this material is much larger than the grain size and in the range of several micrometers, whereas very often the dimple size of UFG and NC metals is only in the order of a couple grain

diameters [51]. The limited dimple size controls the maximum CTOD and lastly the fracture toughness.

A distinctive difference in fracture toughness in absolute numbers exists for the radial direction. A similar increase in fracture toughness was seen before for iron in this orientation and the explanation for that was based on the formation of delaminations in this orientation which are known to have a beneficial effect on fracture toughness. However, in the present case such delaminations do not form in Ti45Nb and the failure type is again a ductile dimple fracture, see Fig. 6. The mechanistic origin for the higher fracture toughness for this specific orientation is not fully clear at the moment. From the fractographs, see Fig. 6, it can be seen that the dimple size for the radial orientation seems to be larger than for the other two testing orientation, which implies a difference in the void growth mechanism that postpones the critical CTOD to larger crack tip deformations. For void initiation and growth, triple junctions are known to play an important role in UFG and NC metals. Therefore, a further analysis of the distribution and frequency of the void initiation sites ahead of the crack tip in relation to the 3-dimensional shape of the grains might bear further insights into the origin of the fracture toughness anisotropy.

Summary

In the present study HPT was successfully applied on relatively large samples that could be of interest for small implants for example used in the dentistry field. Using HPT a substantial increase of strength of about 250 % without a change of the crystal structure or the formation of new phases could be achieved. The ductility remained sufficiently high and the fracture toughness decreased only to about 70 % of the soft coarse-grained material [50]. In addition, strength and fracture toughness exhibit a pronounced orientation dependence. This is only weakly pronounced as regards strength and more pronounced for the fracture toughness. The property enhancement through HPT-processing makes Ti45Nb to a good candidate material for load bearing implants.

Acknowledgements

The authors would like to thank Prof. Reinhard Pippan from the Erich Schmid Institute for the helpful discussions. Funding of this work has been provided by the European Research Council under ERC Grant Agreement No. 340185 USMS and by the FWF Austrian Science Fund within project number P26729-N19. Additional funding by the European Commission within the framework of the FP7-ITN Network BioTiNet (PITN-GA-2010-264635) and the Deutsche Forschungsgemeinschaft (DFG) in the framework of SFB/Transregio 79, project M1 is gratefully acknowledged.

References

- [1] M. Niinomi, Recent research and development in titanium alloys for biomedical applications and healthcare goods, *Sci. Technol. Adv. Mater.* 4 (2003) 445.
- [2] M. Niinomi, Biologically and Mechanically Biocompatible Titanium Alloys, *Mater. Trans.* 49 (2008) 2170–2178.
- [3] M. Niinomi, M. Nakai, Titanium-Based Biomaterials for Preventing Stress Shielding between Implant Devices and Bone, *Int. J. Biomater.* 2011 (2011) 1–10.
- [4] M. Long, H.J. Rack, Titanium alloys in total joint replacement—a materials science perspective, *Biomaterials.* 19 (1998) 1621–1639.
- [5] H.K. Uthoff, F.L. Dubuc, Bone structure changes in the dog under rigid internal fixation., *Clin. Orthop.* 81 (1971) 165–170.
- [6] W.H. Akeson, S.L.Y. Woo, R.D. Coutts, J.V. Matthews, M. Gonsalves, D. Amiel, Quantitative histological evaluation of early fracture healing of cortical bones immobilized by stainless steel and composite plates, *Calcif. Tissue Res.* 19 (1975) 27–37.
- [7] R.M. Pilliar, H.U. Cameron, A.G. Binnington, J. Szivek, I. Macnab, Bone ingrowth and stress shielding with a porous surface coated fracture fixation plate, *J. Biomed. Mater. Res.* 13 (1979) 799–810.
- [8] D. Kuroda, M. Niinomi, M. Morinaga, Y. Kato, T. Yashiro, Design and mechanical properties of new β type titanium alloys for implant materials, *Mater. Sci. Eng. A.* 243 (1998) 244–249.
- [9] M. Niinomi, T. Hattori, K. Morikawa, T. Kasuga, A. Suzuki, H. Fukui, et al., Development of Low Rigidity β -type Titanium Alloy for Biomedical Applications, *Mater. Trans.* 43 (2002) 2970–2977.
- [10] R.Z. Valiev, Y. Estrin, Z. Horita, T.G. Langdon, M.J. Zehetbauer, Y.T. Zhu, Fundamentals of Superior Properties in Bulk NanoSPD Materials, *Mater. Res. Lett.* 4 (2016) 1–21.
- [11] S.G. Fedotov, P.K. Belousov, Elastic constants of the system titanium-niobium, *Fiz Met Met.* 17 (1964) 732–736.
- [12] S. Hanada, T. Ozaki, E. Takahashi, S. Watanabe, K. Yoshimi, T. Abumiya, Composition dependence of Young's modulus in beta titanium binary alloys, 2003.
- [13] T. Ozaki, H. Matsumoto, S. Watanabe, S. Hanada, Beta Ti Alloys with Low Young's Modulus, *Mater. Trans.* 45 (2004) 2776–2779.
- [14] M. Niinomi, Mechanical properties of biomedical titanium alloys, *Mater. Sci. Eng. A.* 243 (1998) 231–236.
- [15] M. Niinomi, T. Hattori, K. Morikawa, T. Kasuga, A. Suzuki, H. Fukui, et al., Development of Low Rigidity β -type Titanium Alloy for Biomedical Applications, *Mater. Trans.* 43 (2002) 2970–2977.
- [16] R.Z. Valiev, R.K. Islamgaliev, I.V. Alexandrov, Bulk nanostructured materials from severe plastic deformation, *Prog. Mater. Sci.* 45 (2000) 103–189.
- [17] Y. Estrin, A. Vinogradov, Extreme grain refinement by severe plastic deformation: A wealth of challenging science, *Acta Mater.* 61 (2013) 782–817.
- [18] R. Valiev, Nanostructuring of metals by severe plastic deformation for advanced properties, *Nat. Mater.* 3 (2004) 511–516.
- [19] R.Z. Valiev, Y. Estrin, Z. Horita, T.G. Langdon, M.J. Zechetbauer, Y.T. Zhu, Producing bulk ultrafine-grained materials by severe plastic deformation, *JOM.* 58 (2006) 33–39.
- [20] A.V. Sergueeva, V.V. Stolyarov, R.Z. Valiev, A.K. Mukherjee, Advanced mechanical properties of pure titanium with ultrafine grained structure, *Scr. Mater.* 45 (2001) 747–752.
- [21] C.N. Elias, M.A. Meyers, R.Z. Valiev, S.N. Monteiro, Ultrafine grained titanium for biomedical applications: An overview of performance, *J. Mater. Res. Technol.* 2 (2013) 340–350.
- [22] Y. Estrin, H.-E. Kim, R. Lapovok, H.P. Ng, J.-H. Jo, Mechanical Strength and Biocompatibility of Ultrafine-Grained Commercial Purity Titanium, *BioMed Res. Int.* 2013 (2013) 1–6.

- [23] H. Yilmazer, M. Niinomi, M. Nakai, K. Cho, J. Hieda, Y. Todaka, et al., Mechanical properties of a medical β -type titanium alloy with specific microstructural evolution through high-pressure torsion, *Mater. Sci. Eng. C*. 33 (2013) 2499–2507.
- [24] R.K. Islamgaliev, V.U. Kazyhanov, L.O. Shestakova, A.V. Sharafutdinov, R.Z. Valiev, Microstructure and mechanical properties of titanium (Grade 4) processed by high-pressure torsion, *Mater. Sci. Eng. A*. 493 (2008) 190–194.
- [25] Y.C. Wang, T.G. Langdon, Effect of heat treatment on microstructure and microhardness evolution in a Ti–6Al–4V alloy processed by high-pressure torsion, *J. Mater. Sci.* 48 (2012) 4646–4652.
- [26] A. Panigrahi, M. Bönisch, T. Waitz, E. Schafner, M. Calin, J. Eckert, et al., Phase transformations and mechanical properties of biocompatible Ti–16.1Nb processed by severe plastic deformation, *J. Alloys Compd.* 628 (2015) 434–441.
- [27] C.M. Lee, C.P. Ju, J.H. Chern Lin, Structure–property relationship of cast Ti–Nb alloys, *J. Oral Rehabil.* 29 (2002) 314–322.
- [28] A. Panigrahi, B. Sulkowski, T. Waitz, K. Ozaltin, W. Chrominski, A. Pukenas, et al., Mechanical properties, structural and texture evolution of biocompatible Ti–45Nb alloy processed by severe plastic deformation, *J. Mech. Behav. Biomed. Mater.* 62 (2016) 93–105.
- [29] A. Hohenwarter, R. Pippan, Anisotropic fracture behavior of ultrafine-grained iron, *Mater. Sci. Eng. A*. 527 (2010) 2649–2656.
- [30] A. Hohenwarter, R. Pippan, Fracture of ECAP-deformed iron and the role of extrinsic toughening mechanisms, *Acta Mater.* 61 (2013) 2973–2983.
- [31] A.P. Zhilyaev, T.G. Langdon, Using high-pressure torsion for metal processing: Fundamentals and applications, *Prog. Mater. Sci.* 53 (2008) 893–979.
- [32] A. Vorhauer, R. Pippan, On the homogeneity of deformation by high pressure torsion, *Scr. Mater.* 51 (2004) 921–925.
- [33] T. Hebesberger, H.P. Stüwe, A. Vorhauer, F. Wetscher, R. Pippan, Structure of Cu deformed by high pressure torsion, *Acta Mater.* 53 (2005) 393–402.
- [34] R. Pippan, S. Scheriau, A. Taylor, M. Hafok, A. Hohenwarter, A. Bachmaier, Saturation of Fragmentation During Severe Plastic Deformation, *Annu. Rev. Mater. Res.* 40 (2010) 319–343.
- [35] ASTM E399-90. Standard test method for plane-strain fracture toughness of metallic materials, American Society of Testing and Materials, Philadelphia (PA), 1990.
- [36] G.B. Rathmayr, A. Bachmaier, R. Pippan, Development of a New Testing Procedure for Performing Tensile Tests on Specimens with Sub-Millimetre Dimensions, *J. Test. Eval.* 41 (2013) 20120175.
- [37] O. Kolednik, H.P. Stüwe, The stereophotogrammetric determination of the critical crack tip opening displacement, *Eng. Fract. Mech.* 21 (1985) 145–155.
- [38] J. Stampfl, S. Scherer, M. Berchthaler, M. Gruber, O. Kolednik, Determination of the fracture toughness by automatic image processing, *Int. J. Fract.* 78 (1996) 35–44.
- [39] T.L. Anderson, *Fracture Mechanics: Fundamentals and Applications*, Third Edition, CRC Press, 2005.
- [40] A. Hohenwarter, A. Bachmaier, B. Gludovatz, S. Scheriau, R. Pippan, Technical parameters affecting grain refinement by high pressure torsion, *Int. J. Mater. Res.* 100 (2009) 1653–1661.
- [41] R.B. Figueiredo, T.G. Langdon, Development of structural heterogeneities in a magnesium alloy processed by high-pressure torsion, *Mater. Sci. Eng. A*. 528 (2011) 4500–4506.
- [42] B.W. Levinger, Lattice parameters of beta titanium, *J. Met.* 5 (1953) 195.
- [43] R. Pippan, S. Scheriau, A. Taylor, M. Hafok, A. Hohenwarter, A. Bachmaier, Saturation of Fragmentation During Severe Plastic Deformation, *Annu. Rev. Mater. Res.* 40 (2010) 319–343.
- [44] N. Krasilnikov, W. Lojkowski, Z. Pakiel, R. Valiev, Tensile strength and ductility of ultra-fine-grained nickel processed by severe plastic deformation, *Mater. Sci. Eng. A*. 397 (2005) 330–337.
- [45] N. Lugo, N. Llorca, J.M. Cabrera, Z. Horita, Microstructures and mechanical properties of pure copper deformed severely by equal-channel angular pressing and high pressure torsion, *Mater. Sci. Eng. A*. 477 (2008) 366–371.

- [46] R.Z. Valiev, N.A. Enikeev, M.Y. Murashkin, V.U. Kazykhanov, X. Sauvage, On the origin of the extremely high strength of ultrafine-grained Al alloys produced by severe plastic deformation, *Scr. Mater.* 63 (2010) 949–952.
- [47] T. Saito, Multifunctional Alloys Obtained via a Dislocation-Free Plastic Deformation Mechanism, *Science*. 300 (2003) 464–467.
- [48] I. Sabirov, R.Z. Valiev, I.P. Semenova, R. Pippan, Effect of Equal Channel Angular Pressing on the Fracture Behavior of Commercially Pure Titanium, *Metall. Mater. Trans. A.* 41 (2010) 727–733.
- [49] I. Sabirov, R.Z. Valiev, R. Pippan, About application of three dimensional analyses of fracture surfaces in fracture study on nanostructured titanium, *Comput. Mater. Sci.* 76 (2013) 72–79.
- [50] T.S. Byun, S.-H. Kim, J. Mammosser, Low-temperature mechanical properties of superconducting radio frequency cavity materials, *J. Nucl. Mater.* 392 (2009) 420–426.
- [51] A. Pineau, A. Amine Benzerga, T. Pardoen, Failure of metals III: Fracture and fatigue of nanostructured metallic materials, *Acta Mater.* 107 (2016) 508–544.

Figure captions

Figure 1 a) Orientation of the different compact tension (CT) and tensile samples extracted from the HPT disk. b) Geometry of the C(T) samples. c) Geometry of the tensile samples having a diameter d of about 500 μm and a gauge length of about 3 mm.

Figure 2 Inverse pole figure map of the as-received material.

Figure 3 Hardness measurements performed on the deformed HPT disk. Hardness measurements were performed along the radius from the center to the edge and across the thickness of the disk. The inset image represents the cross-section of the disk showing the planes and their distance from the middle plane along which the hardness was tested. The saturation regime with about 2.6 GPa for the middle plane of the disk is reached in about 1 mm radial distance from the center.

Figure 4 In a) a bright-field STEM image and in c) a HAADF STEM image of the saturation region are depicted. Both images show the as-deformed state after the HPT deformation with elongated grains which have a thickness of about 50 nm. In b) the diffraction pattern of the as-deformed state is depicted, which shows a single phased β -Ti bcc structure.

Figure 5 Stress-strain curves for the as-received state and the HPT-deformed state in two directions (axial and shear). A significant increase in strength is seen for the as-deformed samples compared to the initial state.

Figure 6 Examples of CTOD_i measurement for all three testing orientations taken at the crack initiation site. Comparison of fractographs taken from the two halves of the broken specimen at the same position with indicated identical crack paths along which the CTOD_i was measured (left sides). Arrangement of the crack profiles at the point prior to coalescence of first void defining CTOD_i .

Figure 1 (1 Column)

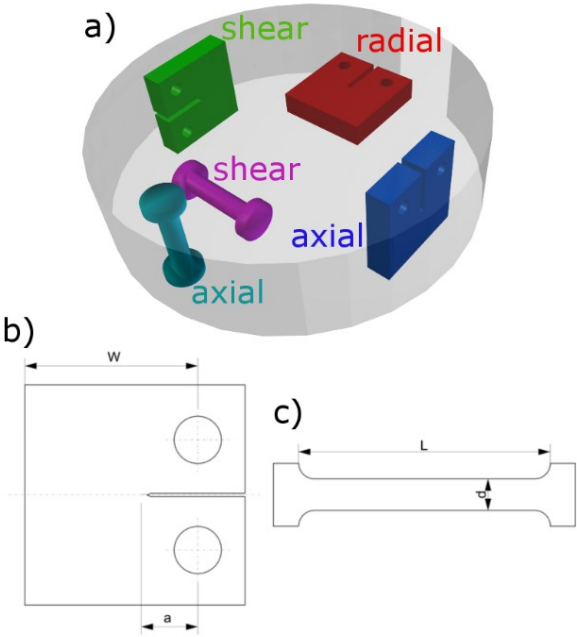


Figure 2 (1 Column)

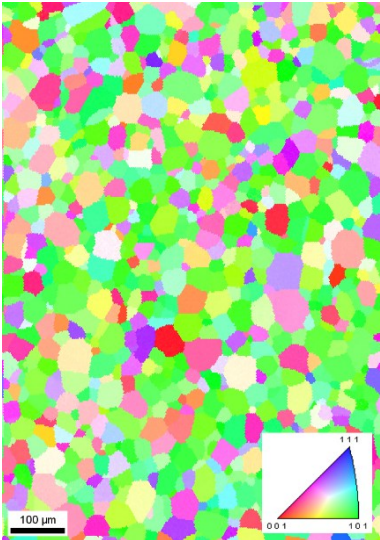


Figure 3 (1.5 Column)

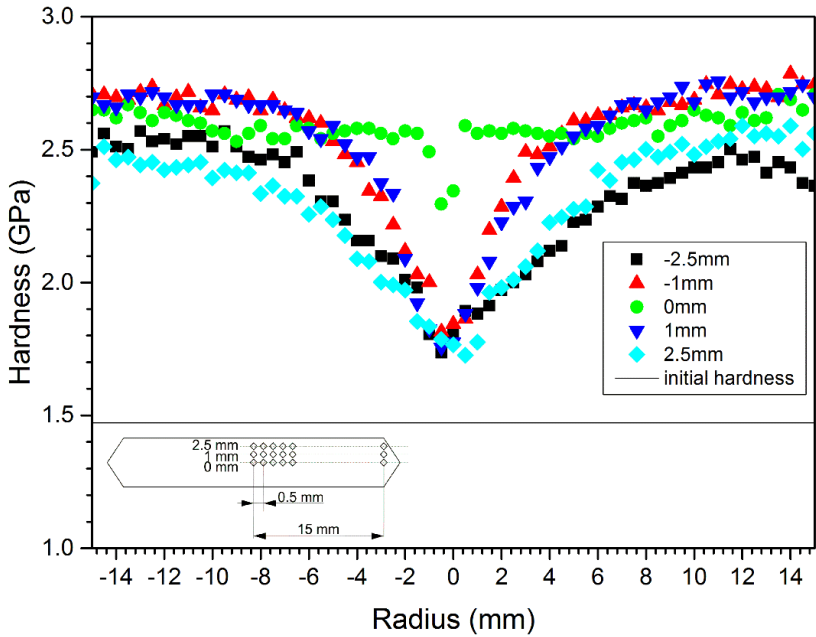


Figure 4 (1.5 Column)

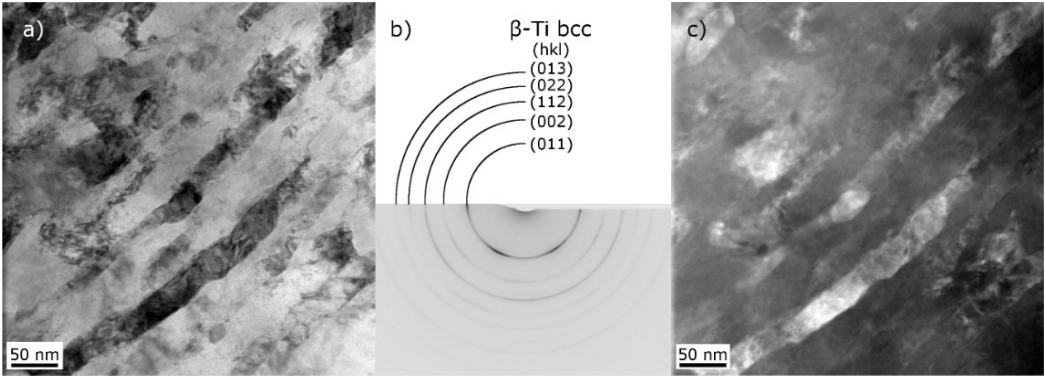


Figure 5 (1 Column)

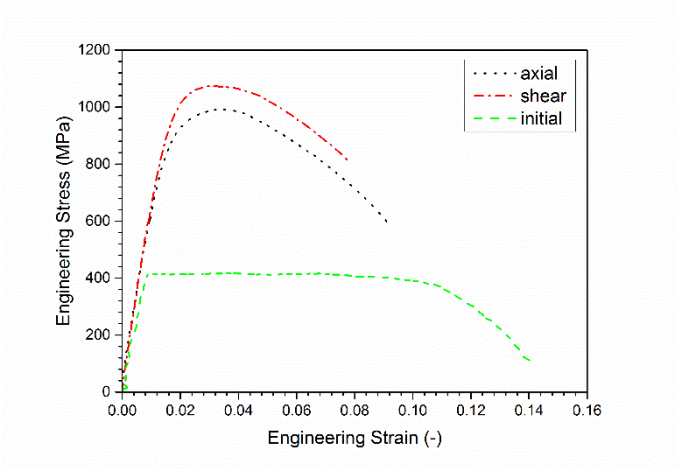
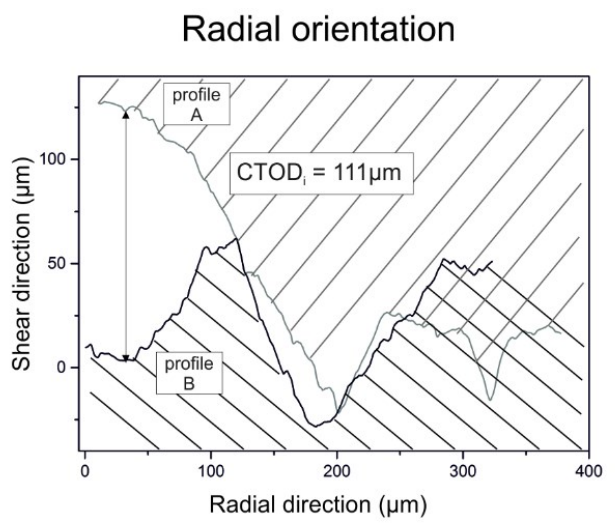
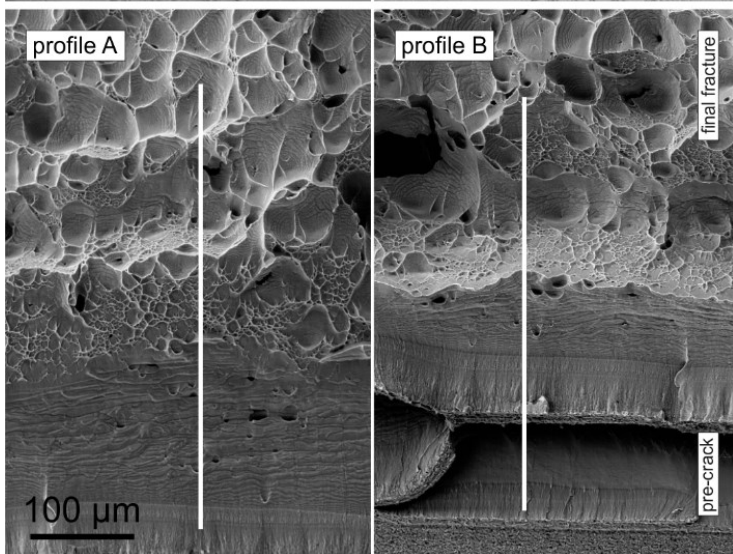
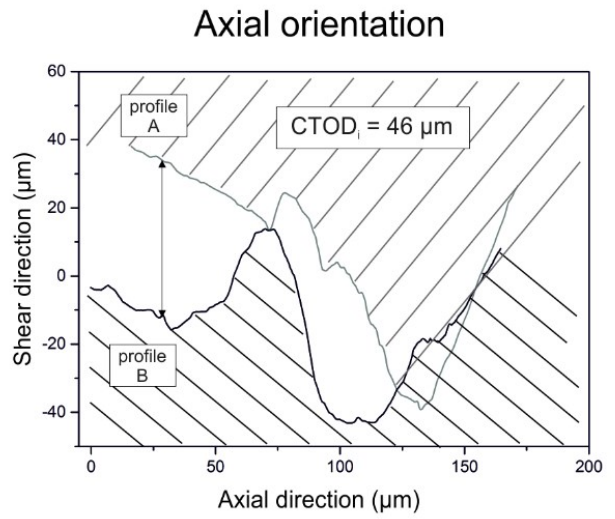
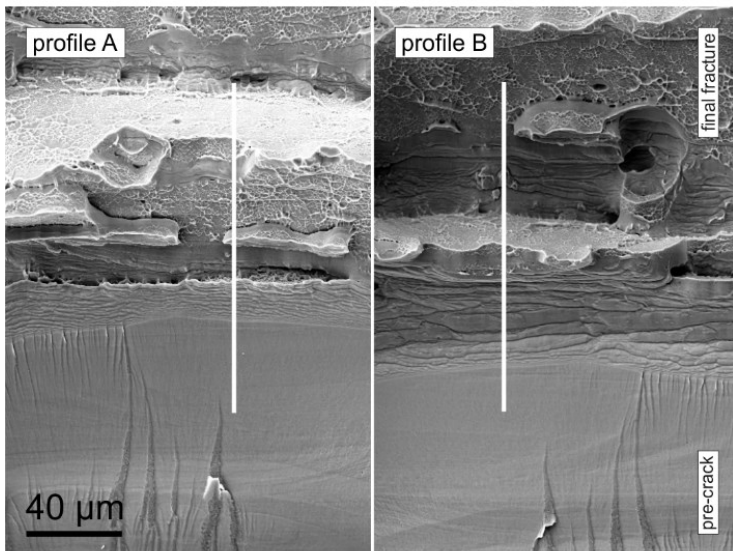
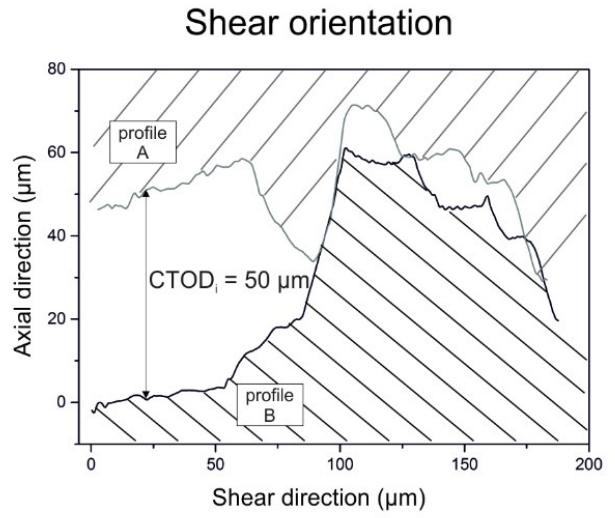
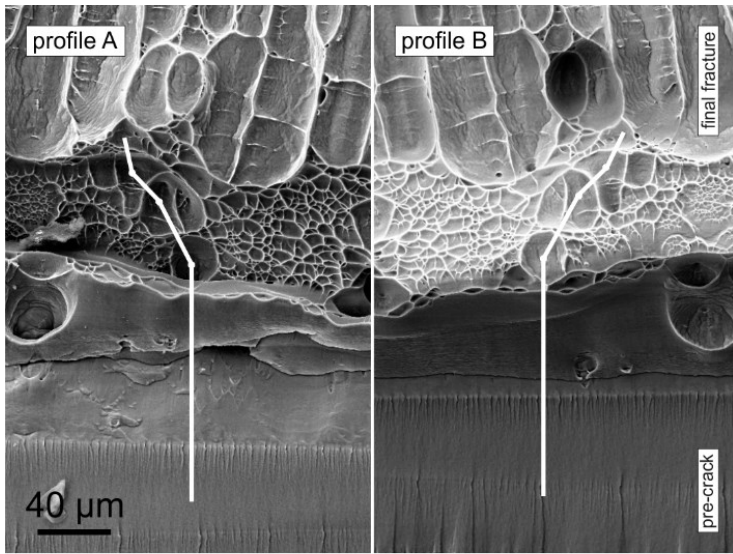


Figure 6 (2 Column)



Tables

Table 1 Summary of the results of the tensile test. $R_{p0.2}$ represents the yield strength, R_m the ultimate tensile strength, A_m the uniform elongation and A_f the elongation to fracture. The values represent average numbers of 3 measurements and as an error the standard deviation is given.

Orientation	as-received	axial	shear
$R_{p0.2}$ (MPa)	354±38	800±25	896±52
R_m (MPa)	418±41	948±28	1046±26
A_m (%)	6.8±0.2	1.3±0.3	1.4±0.1
A_f (%)	13.8±0.2	7.1±1.0	7.6±1.1

Table 2 Overview of the fracture toughness results for different testing orientations: Calculated fracture toughness value K_Q according to ASTM E399-90, the maximum fracture toughness, K_{max} , derived from the maximum load, the force-ratio, P_{max}/P_Q , of maximum force and the force used for K_Q -calculation, the crack tip opening displacement for crack initiation (CTOD_i) and fracture toughness, K_{IC} , calculated from CTOD_i.

Orientation	axial	radial	shear
K_Q (MPa√m)	21	25	42
K_{max} (MPa√m)	61	58	64
P_{max}/P_Q (-)	2.9	2.3	1.5
CTOD _i (μm)	40	106	49
K_{IC} (from CTOD) (MPa√m)	74	109	78